**Fig. 1.** Principle of the proposed method.

Since the particle velocity is continuous at the boundary between media with different acoustic impedances, the particle velocity on the surface boundary of a sample is equivalent to that inside the sample. On the basis of the above assumptions and another assumption that the entire cartilage tissue sample is homogeneous, when only the plane progressive wave of a longitudinal wave propagates in the homogeneous cartilage sample, the particle velocity $v_i$ is expressed as

$$v_i = \sqrt{2}v_i' e^{j\omega_0 t}, \qquad (1)$$

where $v_i'$, $\omega_0$, and $t$ indicate the effective value of particle velocity, angular frequency, and time, respectively. The index $i$ of $v_i'$ means the incident wave, that is, the progressive wave in the sample. The effective value of particle velocity $v_i'$ is expressed as follows, by using the effective value of velocity potential $\phi_i'$ $(= |\phi_i'|e^{-jkx})$:

$$v_i' = jk\phi_i', \qquad (2)$$

where $k$ $(= \omega_0/c)$ is the wavelength constant, $x$ indicates the propagation direction of the plane wave, and $c$ is the sound speed of the longitudinal wave in the sample.

Next, the particle displacement $u_i$ is derived as follows, by integrating the particle velocity $v_i$ with respect to time:

$$u_i = \sqrt{2}u_i' e^{j\omega_0 t}, \qquad (3)$$

where $u_i'$ is the effective value of particle displacement and is expressed as follows:

$$u_i' = \frac{1}{c}\phi_i', \qquad (4)$$

where $u_i'$ is a function of $x$. To attain elasticity information, strain $\varepsilon_i'$ is derived as follows, by differentiating $u_i'$ with respect to $x$:

$$\varepsilon_i' = -j\frac{k}{c}\phi_i'. \qquad (5)$$

The above particle displacement and strain are induced by local stress along the propagation direction of a plane wave

in the acoustic field. Assuming that the stress in the inside and boundary of the sample is induced by an incident wave in the sample, the stress $\sigma_i'$ is expressed as follows:

$$\sigma_i' = j\omega_0\rho\phi_i', \qquad (6)$$

where $\rho$ is the density of the sample. On the basis of the one-dimensional (1D) elastic equation, the bulk modulus $K$ is derived as follows, by calculating the ratio of the stress $\sigma_i'$ to strain $\varepsilon_i'$:

$$K = \frac{|\sigma_i'|}{|\varepsilon_i'|}. \qquad (7)$$

Actually, since the laser Doppler measurement in Fig. 1 is conducted at only one point on the surface boundary of the sample, the above-mentioned strain $|\varepsilon_i'|$ is approximated as follows, by using the simultaneously measured sample thickness $l$:

$$|\varepsilon_i'| = \frac{|u_i'|}{l}. \qquad (8)$$

This processing corresponds to the calculation of the average strain in the inside of a sample, when it is assumed that the displacement at the bottom boundary of the sample is zero.

When the stress $|\sigma_i'|$ is constant and the sample has the thickness in which the influence of attenuation is negligible, the inverse of strain (IS), $1/|\varepsilon_i'|$, is proportional to the bulk modulus $K$. The bulk modulus $K$ can be expressed as $K = E/[3(1 - 2\nu)]$, by using Young's modulus $E$ and Poisson's ratio $\nu$ in the isotropic and linear elastic body. Therefore, since the IS has the potential to evaluate elasticity, the IS is used as the elasticity evaluation index in this paper. In the following sections, the feasibility of the proposed method for regenerating cartilage samples is investigated.

## 3. Measurement System

Figure 2 shows the measurement system used in this study. A cylindrical sample tank contained phosphate buffered saline (PBS) whose temperature was kept at 20.0 °C. In the sample tank, a circular urethane-based acoustic coupler (Takiron STD112) with a thickness of 10 mm and a diameter of 20 mm was put on the surface of an ultrasound transducer with a planar aperture, a center frequency of 1 MHz, and a circular element with a diameter of 6 mm (GE Sensing and Inspection Tech. 221-340), and an extracted regenerating cartilage sample was put on the acoustic coupler. Here, the density and sound speed of the acoustic coupler were $1.01 \times 10^3$ kg/m$^3$ and 1519 m/s, respectively, where the density was determined by measuring the increment in the volume of water when immersing the coupler in the water and the weight of the coupler, and the sound speed was determined by measuring the round-trip propagation time of multiple echoes through the inside of the coupler and the thickness of the coupler. A laser Doppler vibrometer (LDV; Graphtec AT0023 and AT3700) with a spot diameter of 20 μm and frequency ranges up to 10 MHz was set up 30 cm away from the cartilage sample surface. The spot of LDV was also positioned on the central axis of the acoustic field, by irradiating a visible red laser beam (wavelength: 632.8 nm) on the aperture center of the ultrasound transducer before putting the coupler on the transducer. On the basis of such settings, since the central axis of the acoustic field can
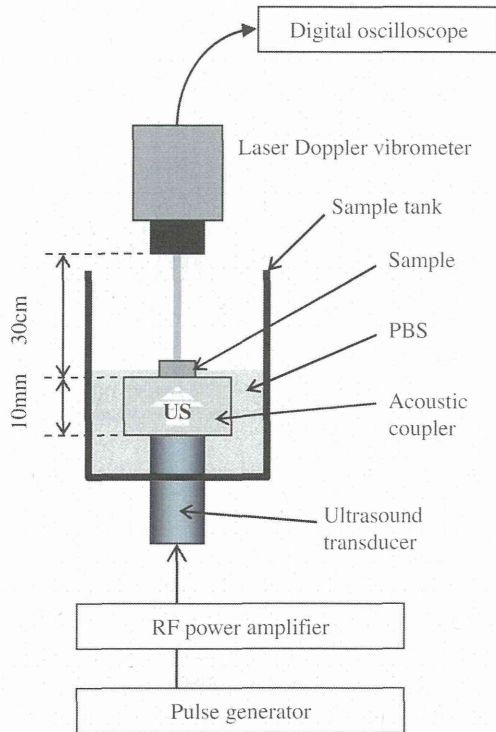
**Fig. 2.** Setup for laser Doppler measurement of ultrasound particle velocity.



**Fig. 3.** Simulated acoustic field in the experimental setup: (a) acoustic field and (b) wavefront distribution.

be identified by observing the position of the visible laser spot, the central axis of the acoustic field can be easily placed on the center position of the sample.

On the other hand, the thickness of the acoustic coupler was determined by acoustic field simulation using the Rayleigh formula in a homogeneous medium. In this simulation, the acoustic field is calculated from the surface integral of spherical wave radiation on the above transducer aperture. Since this study considered only the small region of acoustic field around the central axis, no generations of shear wave and surface acoustic wave were considered in this simulation. Figures 3(a) and 3(b) show the calculated acoustic field and wavefront distribution obtained by the phase calculation. In Fig. 3(a), a field more distant than 10 mm from the surface of ultrasound transducer is a far field. In the far field, although the wavefront is uniform along the lateral direction, it is predicted that the stress is not uniform along the lateral direction and exhibits a maximum value on the central axis. However, from the result of this simulation, the variation of amplitude along the lateral direction to the maximum amplitude on the central axis at a depth of 10 mm was 0.002% within a spot diameter of 20 μm in the LDV. Therefore, in this paper, it is assumed that the plane wave approximation is valid within the spot diameter of the LDV around the central axis of a far field.

After finishing the above setup, a pulsed-wave ultrasound with five cycles was irradiated to the bottom of the cartilage sample via the acoustic coupler. The applied voltage to the ultrasound transducer was 450 $V_{pp}$ and was maintained constant. This acoustic output which arises from this applied voltage generates the particle displacement of 0.46 μm on the surface of the acoustic coupler, which was obtained by
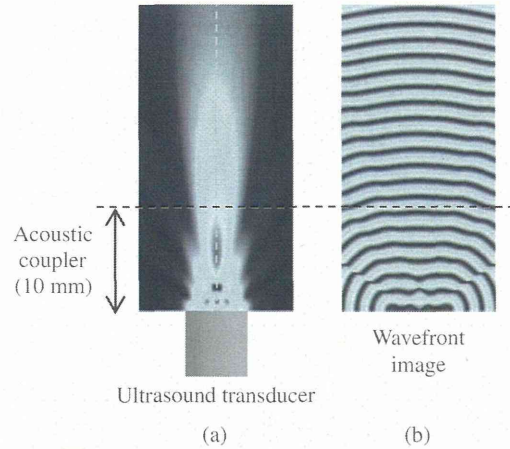
the following root mean square (RMS) calculation for the particle displacement waveform on the surface of the acoustic coupler. Then, the LDV was used to measure the ultrasound particle velocity on the surface of the cartilage sample, and the particle velocity waveforms were recorded using a digital oscilloscope (LeCroy WS454VL) at a sampling frequency of 500 MHz. After recording the data, the particle velocity waveform is converted to the particle displacement waveform by temporal integration. Then, $|u_i'|$ in eq. (8) is attained by calculating the RMS of the particle displacement waveform. The calculation of RMS is also effective for obtaining a high signal-to-noise ratio. At the same time, the thickness of the sample, $l$ in eq. (8), was also measured using a laser thickness indicator (Keyence LK-G35). Finally, the IS, that is, $1/|\varepsilon_i'|$, was calculated using eq. (8), and the elasticity of the regenerating cartilage sample was evaluated using the IS.

The obtained IS was compared with the Young's modulus measured by the static compression test. After IS measurement, the static compression test was conducted using an Instron-type universal testing machine (A&D UTM-10T). The sample was quasistatically compressed by a plate-type indenter with a diameter of 10 mm at a constant crosshead speed of 2 mm/min, and at the same time, the compression forces were measured using a load cell (rating capacity of 1 kg, resolution of 0.02% of rating capacity). Stress and strain were calculated from the measured forces and the dimensions of the sample, and then the Young's modulus of the sample was calculated using the ratio of stress to strain. Here, while the IS reflects the bulk modulus, the Young's modulus is measured in the the static compression test. However, under the assumption that Poisson's ratio is constant, the bulk modulus is proportional to the Young's modulus. Therefore, in the following experiments, the Young's modulus was referred to for verifying the capability of IS in the elasticity evaluation.

## 4. Phantom Experiment

To investigate the feasibility of this method for distinguishing the elasticity of a sample, three homogeneous phantoms with different elasticities (0.05, 0.1, 0.2 MPa as Young's
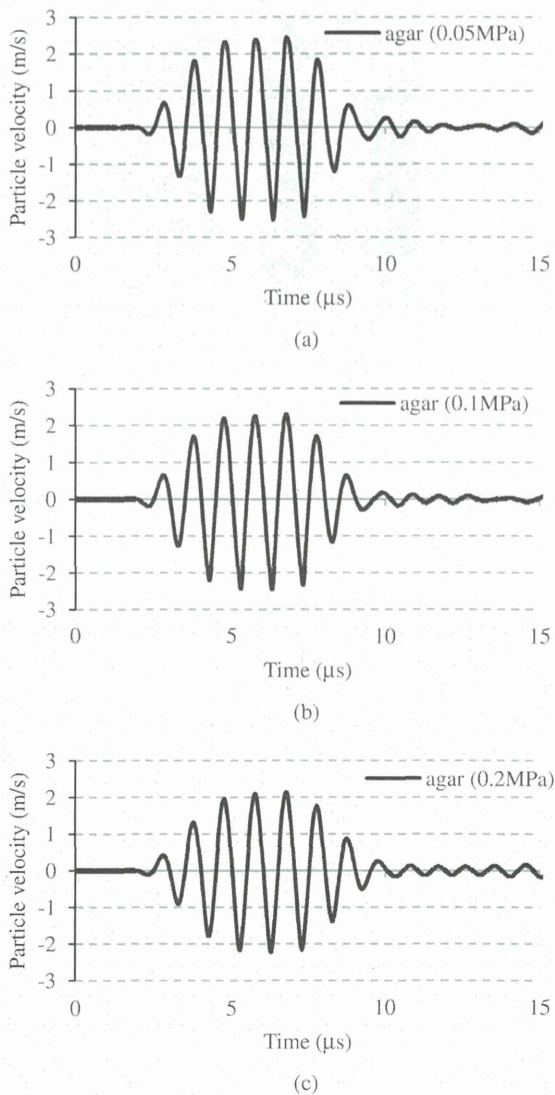
(a)



(b)



(c)

**Fig. 4.** Examples of particle velocity waveforms on the surface of agar-based phantoms: (a) 0.05, (b) 0.1, and (c) 0.2 MPa.



Number of measurements (upper values) and Young's modulus (lower values)

**Fig. 5.** Particle displacement values on the surface of agar-based phantoms.

modulus) and a constant size (each side of 10 mm, thickness of 5 mm) were formed by changing the weight concentration of agar powder. The Young's moduli of these phantoms were measured by the static compression test described in §3. Since the weight concentration of agar powder correlates with its elasticity, the three phantoms simulate the temporal elasticity change according to the maturity of the regenerating cartilage sample. Here, the densities of the agar-based phantoms with Young's moduli of 0.05, 0.1, and 0.2 MPa were $1.01 \times 10^3$, $1.02 \times 10^3$, and $1.02 \times 10^3$ kg/m$^3$, respectively. Likewise, the sound speeds of the agar-based phantoms with Young's moduli of 0.05, 0.1, and 0.2 MPa were 1520, 1532, and 1556 m/s, respectively. These densities and sound speeds were measured by using the density and sound speed measurement methods of the acoustic coupler as described in §3.

Each phantom was put on the acoustic coupler, and the laser spot was placed at the center position of the phantom surface. As mentioned in §3, since the magnitude of stress is not uniform along the lateral direction and exhibits a
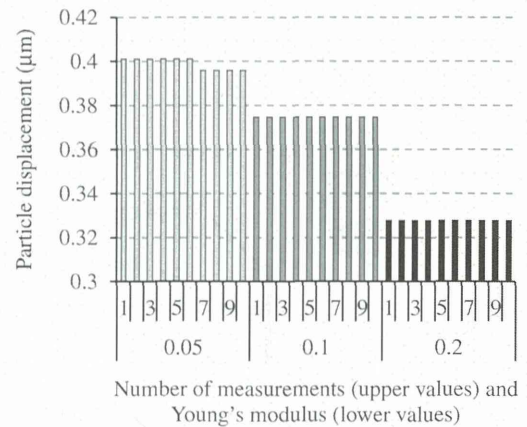
maximum value on the central axis, it is predicted that the particle velocity measured by the LDV is affected by the spot positioning. However, in this study, the spot is always placed on the central axis of the acoustic field, and the plane wave approximation is valid within the spot diameter of the LDV around the central axis of the far field. Therefore, in a homogeneous phantom, the particle velocity measurement is not affected by the stress distribution along the lateral direction.

Figure 4 shows examples of particle velocity waveforms measured by the LDV. As the elasticity of the agar-based phantom increases, a slight decrease in waveform amplitude can be observed. Figure 5 shows the RMS values of particle displacement waveforms on the surface of each phantom. The horizontal axis indicates the number of measurements on the same surface point of each phantom (upper values) and the Young's modulus variation (lower values). Since the thickness of each phantom was constant, the displacement decreased with the increase in elasticity. In addition, this result shows that the reproducibility of the measured results is good. Figure 6 shows a comparison between the IS obtained by the method described in §2 and the Young's modulus measured by the static compression test. The tendency of IS coincided well with that of the Young's modulus measured by the static compression test. That is, this method is capable of evaluating sample elasticity.

## 5. Regenerating Cartilage Sample Measurements

*In vitro* measurements using the regenerating cartilage samples (Fig. 7), which were extracted from beagles in approved animal experiments, were conducted by using the above-mentioned system. Autologous auricular cartilage cells of the beagle were transfused into a poly(L-lactic acid) (PLLA) scaffold and cultured during a certain period of time. The scaffolds with the cultured cells were transplanted subcutaneously in the same beagle and extracted after 2 months. Figure 7(a) shows photographs of regenerating cartilage samples extracted after culturing for 1 week (1wk), 2 weeks (2wk), and 3 weeks (3wk). Here, "control" means the cartilage sample regenerated using only the scaffold without any cells. Figure 7(b) shows optical photomicrographs of toluidine blue stain for the samples
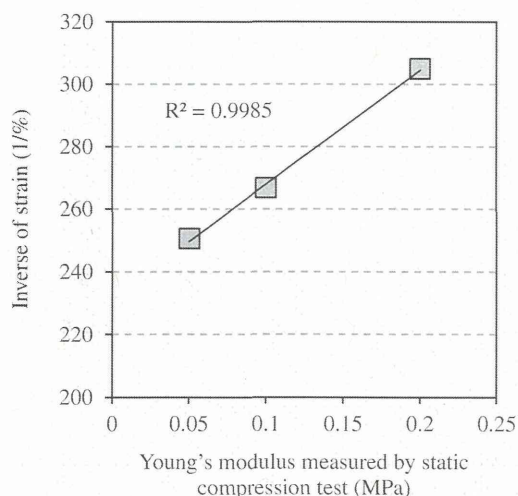
**Fig. 6.** Comparison between inverse of strain (IS) and Young's modulus measured by the static compression test.
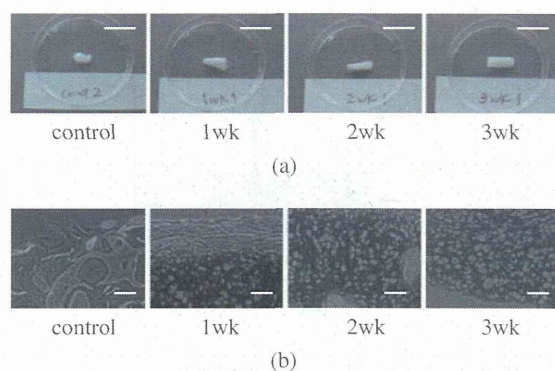


**Fig. 7.** Regenerating cartilage samples extracted from beagles: (a) photographs of regenerating cartilage samples extracted after culturing for 1 week (1wk), 2 weeks (2wk), and 3 weeks (3wk), and "control" means the cartilage sample regenerated using only the scaffold without any cells. Each bar indicates 10 mm length. (b) optical photomicrographs of toluidine blue stain for the samples shown in (a). Each bar indicates 100 μm length.

shown in Fig. 7(a). Here, only the density and sound speed of the native auricular cartilage tissue of the beagle (not shown here) were measurable, because the size of that native cartilage tissue sample was sufficient to measure the density and sound speed by using the density and sound speed measurement methods of the acoustic coupler as described in §3. As the result, the density and sound speed were $1.02 \times 10^3 \, \text{kg/m}^3$ and 1599 m/s, respectively. It can be predicted that the acoustic properties of regenerating cartilage tissue become gradually close to those of native cartilage tissue. Therefore, the acoustic impedance determined using the measured density and sound speed is regarded as the maximum acoustic impedance that the regenerating cartilage tissue used in this study attains. On the other hand, as the minimum acoustic impedance, it is reasonable to assume the acoustic impedance of water because the water content of cartilage tissue is high and the acoustic impedance of cartilage tissue is higher than that of water. Therefore, when the density and sound speed of water are assumed to be $1.00 \times 10^3 \, \text{kg/m}^3$ and 1500 m/s,

respectively, the acoustic impedance of regenerating cartilage tissue used in this study can vary within $1.5 \times 10^6$ to $1.64 \times 10^6 \, \text{kg/(m}^2 \cdot \text{s)}$. The extracted cartilage sample (width of 5 mm, thickness of 1 mm) was placed on the acoustic coupler, and the elasticity was evaluated using IS, as well as the above phantom measurements. The LDV spot was also placed on the center position of the regenerating cartilage sample surface. Since the wavelength in the regenerating cartilage sample is predicted to be about 1.6 mm, which is larger than the thickness of the sample, the obtained IS corresponds to the average value along the thickness direction.

Figure 8 shows examples of particle velocity waveforms on the regenerating cartilage sample surface measured using the LDV. As the culture period increases, a slight decrease in the maximum amplitude in the primary waveform located at 5 to 13 μs was observed. Considering the thicknesses of the coupler and sample, the smaller-amplitude waves at approximately 15 μs in Figs. 8(a)–8(c) are the reflection waves in the inside of the coupler and sample, are not the progressive waves intended for elasticity evaluation. Therefore, the RMS calculations for obtaining IS were conducted in the above primary waveform within a constant duration considering the pulse width, and these smaller-amplitude waveforms are not included in the RMS calculations.

Figure 9 shows the IS of regenerating cartilage samples according to the culture periods of 1, 2, and 3 weeks. Again, "control" means the cartilage sample regenerated using only the scaffold without any cells. At the measuring position in this experiment, the IS values of regenerating cartilage samples increased with an increase in the culture period. In addition, these IS values also increased with an increase in the Young's modulus of regenerating cartilage samples measured by the static compression test (for example, 2.05 MPa for 1 week, 2.2 MPa for 2 weeks and 2.5 MPa for 3 weeks). Although additional verifications using many regenerating cartilage samples are required for concluding the relationship between the maturity and elasticity of the regenerating cartilage, at least the above results imply that the IS discriminates the differences in elasticity of the regenerating cartilage and that the IS predicts that longer culture periods induce a tendency to regenerate stiffer cartilage tissues.

## 6. Discussion

This method assumes that only the plane progressive wave propagates inside the homogeneous cartilage sample, the sample has the thickness in which the influence of attenuation is negligible, and the stress inside the sample is constant. Actually, however, not only the incident wave but also the reflected wave from the surface boundary of the sample exists in the inside of the sample. In addition, only the applied stress at the boundary between the coupler and cartilage sample is constant. Since the incident wave penetrating inside of the sample is affected by variation of the acoustic impedance of the sample, the stress inside the sample is affected by the acoustic impedance. Here, we discuss the influence of acoustic impedance variation of the sample in the elasticity evaluation, on the basis of a three layer model including a coupler layer, cartilage sample layer, and surrounding air, as shown in Fig. 10.

Fig. 9. Results of inverse of strain (IS) according to the culture periods in the regenerating cartilage sample.



Fig. 10. Three-layer model for investigating the influence of acoustic impedance variation of samples in the proposed elasticity evaluation.
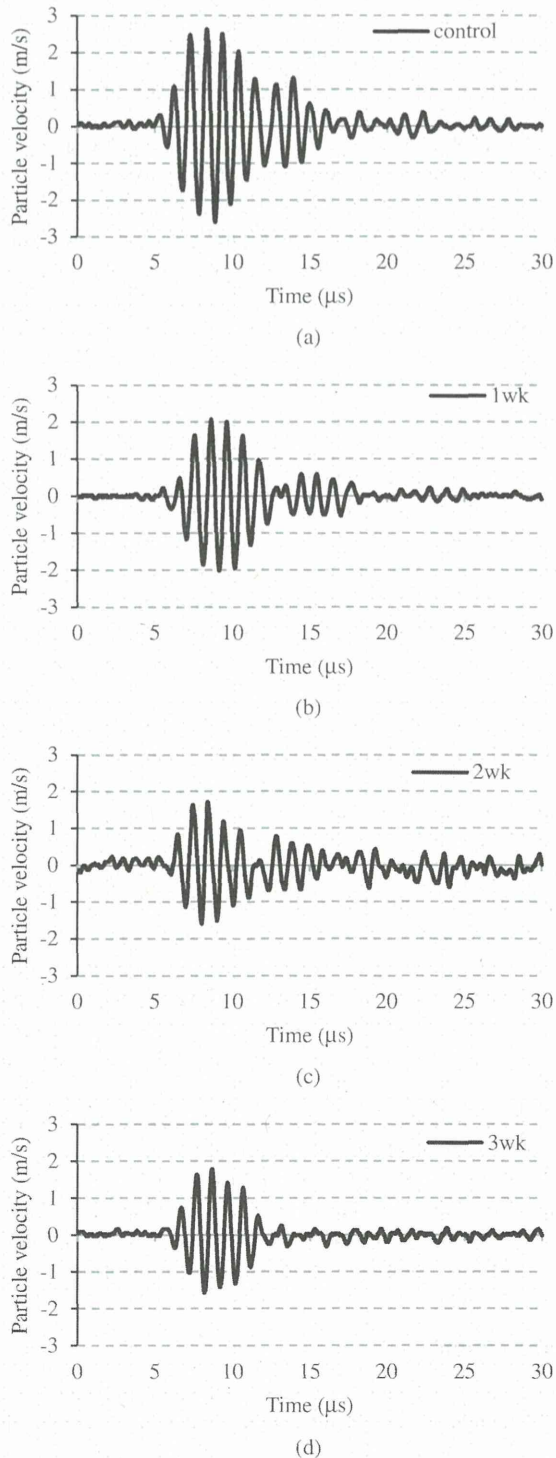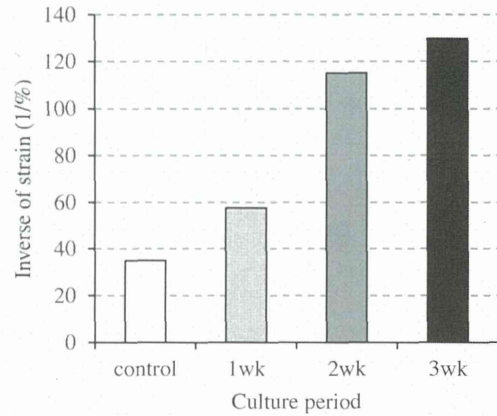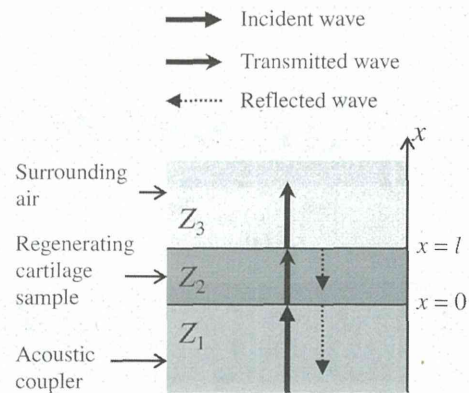
Fig. 8. Examples of particle velocity waveforms on the surface of regenerating cartilage samples: (a) control, (b) 1 week (1wk), (c) 2 weeks (2wk), and (d) 3 weeks (3wk).

In Fig. 10, the coupler layer includes an incident wave and a reflected wave from the boundary of $x = 0$, the cartilage sample layer includes a transmitted wave from the boundary of $x = 0$ and a reflected wave from the boundary of $x = l$, and the surrounding air includes only the transmitted wave from the boundary of $x = l$. The LDV measures particle velocity at $x = l$, and this particle velocity

is equivalent to the particle velocity inside the homogeneous sample, as described in §2. The effective value $v'$ of particle velocity at $x = l$ is expressed as follows, by using the particle velocity component $v'_i$ of the transmitted wave and the particle velocity component $v'_r$ of the reflected wave inside the regenerating cartilage sample:

$$v' = v'_i + v'_r$$
$$= jk(\phi'_i - \phi'_r), \qquad (9)$$

where $\phi'_i$ and $\phi'_r$ are the velocity potential components of the transmitted and reflected waves inside the regenerating cartilage sample, respectively. The effective value $v'_i$ is the same as that shown in eq. (2). From the particle velocity, the strain $\varepsilon'$ at $x = l$ is derived as follows, by using the strain component $\varepsilon'_i$ induced by the transmitted wave and the strain component $\varepsilon'_r$ induced by the reflected wave inside the regenerating cartilage sample:

$$\varepsilon' = \varepsilon'_i + \varepsilon'_r$$
$$= -j\frac{k}{c}(\phi'_i + \phi'_r), \qquad (10)$$

where $\varepsilon'_i$ is the same as that shown in eq. (5). In the actual situation, however, $1/|\varepsilon'|$ is evaluated as IS. In this discussion, $1/|\varepsilon'|$ is referred to as the apparent inverse of strain (AIS) and is distinguished from the IS. Similarly, the

     

stress $\sigma'$ at $x = l$ on the side of the cartilage sample is derived as follows, by using the stress component $\sigma'_i$ induced by the transmitted wave and the stress component $\sigma'_r$ induced by the reflected wave inside the regenerating cartilage sample:

$$\sigma' = \sigma'_i + \sigma'_r$$
$$= j\omega_0\rho(\phi'_i + \phi'_r), \qquad (11)$$

where $\sigma'_i$ is the same as that shown in eq. (6). On the other hand, since only the transmitted wave exists in the surrounding air, the stress $\sigma'_{3i}$ at $x = l$ on the side of the air is derived as follows:

$$\sigma'_{3i} = j\omega_0\rho_3\phi'_{3i}, \qquad (12)$$

where $\rho_3$ is the density of air and $\phi'_{3i}$ is the velocity potential component of the transmitted wave in the air. These stresses are continuous at $x = l$ as follows:

$$\sigma' = \sigma'_{3i}. \qquad (13)$$

Moreover, the stress $\sigma'_{1i}$ at $x = 0$ induced by the incident wave inside the coupler is derived as follows:

$$\sigma'_{1i} = j\omega_0\rho_1\phi'_{1i}, \qquad (14)$$

where $\rho_1$ is the density of the coupler and $\phi'_{1i}$ is the velocity potential component of the incident wave in the coupler. When $\sigma'_i$ and $\varepsilon'_i$ in eq. (7) are replaced by $\sigma'_{1i}$ and $\varepsilon'$, respectively, AIS is derived as follows, by using eqs. (10)–(14):

$$\frac{1}{|\varepsilon'|} = \frac{1}{|\sigma'_{1i}|}\frac{K}{|T_p|}, \qquad (15)$$

where $|T_p|$ is the transmission coefficient of the incident wave inside the coupler, which is defined by the ratio of $\sigma'_{3i}$ to $\sigma'_{1i}$. $|T_p|$ is derived as follows, by using the acoustic impedances $Z_1$, $Z_2$, and $Z_3$ in the layers shown in Fig. 10:

$$|T_p| = \frac{2}{\sqrt{\left(1 + \dfrac{Z_1}{Z_3}\right)^2 \cos^2(kl) + \left(\dfrac{Z_2}{Z_3} + \dfrac{Z_1}{Z_2}\right)^2 \sin^2(kl)}}. \qquad (16)$$

Since only the incident wave inside the coupler is constant, the stress $\sigma'_{1i}$ at $x = 0$ induced by the forementioned incident wave is also constant. Therefore, AIS is proportional to $K/|T_p|$ and is affected by the acoustic impedance variation of the cartilage sample.

To evaluate the influence of $|T_p|$, a calculated result of $K/|T_p|$ to true $K$ is shown in Fig. 11. Here, the horizontal and vertical lines indicate the true $K$ and $K/|T_p|$, respectively. The vertical line corresponds to the AIS. In particular, $K/|T_p|$ was calculated by substituting the acoustic impedance values of the coupler and air ($Z_1 = 1.01 \times 10^3$ [kg/m$^3$] $\times 1519$ [m/s] $= 1.53 \times 10^6$ [kg/(m$^2$·s)], $Z_3 = 1.2$ [kg/m$^3$] $\times 343$ [m/s] $= 412$ [kg/(m$^2$·s)]), frequency (1 MHz), and sample thickness $l$ into eq. (16), and changing the acoustic impedance $Z_2$ of the sample within the realistic range. The thick solid line in Fig. 11 indicates the relationship between $K$ and $K/|T_p|$ in the agar-based phantoms, when the thickness of 5 mm, the density within the range of $1.01 \times 10^3$ to $1.02 \times 10^3$ kg/m$^3$, and the sound speed within the range of 1510 to 1580 m/s are substituted into eq. (16). Here, it was assumed that $K = \rho c^2$. The
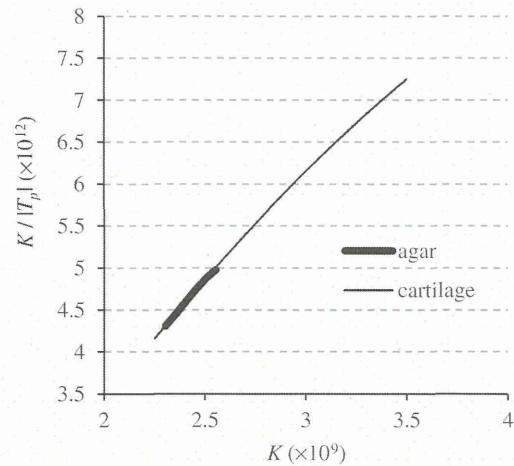


**Fig. 11.** Comparison between true bulk modulus (horizontal line) and bulk modulus affected by the acoustic impedance variation of samples (vertical line).

relationship between $K$ and $K/|T_p|$ is almost linear. In addition, the thin solid line in Fig. 11 indicates the relationship between $K$ and $K/|T_p|$ in the cartilage samples, when the thickness of 1 mm, the density within the range of $1.00 \times 10^3$ to $1.20 \times 10^3$ kg/m$^3$, and the sound speed within the range of 1500 to 1700 m/s are substituted into eq. (16). This acoustic impedance range is wider than that predicted in §5, and the density and sound speed are appropriate for typical cartilage tissues. Again, the relationship between $K$ and $K/|T_p|$ is almost linear. Since the IS is proportional to $K$ and the AIS is also proportional to $K/|T_p|$, consequently, the AIS is proportional to $K$ and IS. Therefore, these relationships imply that AIS can be referred to as IS, and the obtained AIS is usable for elasticity evaluation. Actually, since the experimental results also showed that the relationship between IS and Young's modulus was linear, the feasibility of the proposed method for elasticity evaluation was verified theoretically and experimentally. On the basis of this linear relationship, some appropriate calibrations might enable the quantitative evaluation of elasticity.

On the other hand, eq. (16) includes sinusoidal components (cos and sin). These components are affected by the thickness of the sample, the sound speed of the sample, and the used frequency. However, as shown in Fig. 11, no significant oscillations due to sinusoidal components appear in response to changes in the sound speed of the sample. Therefore, it is important that the appropriate frequency and sample thickness are selected so that the linear relationship between IS and $K$ is maintained within the range of the required elastic modulus and the influence of attenuation is reduced. Consequently, the above discussion showed that the frequency of 1 MHz and sample thickness of 1 or 5 mm in the experiments were appropriate for the elasticity evaluation of a cartilage sample.

## 7. Conclusions

The feasibility of the proposed method was suggested through the phantom and regenerating cartilage sample measurements. Results of experimental and theoretical investigations showed that the IS measured in the proposed

method enabled elasticity evaluations. In a future work, elasticity imaging by scanning the ultrasound beam and the LDV spot simultaneously will be interesting. At the same time, the effectiveness of the proposed method must be verified through measurements of a number of regenerating cartilage samples. Moreover, strategies for *in vivo* measurement of regenerating cartilage must also be investigated.

## Acknowledgments

1) T. Otani, I. Mano, T. Tsujimoto, T. Yamamoto, R. Teshima, and H. Naka: Jpn. J. Appl. Phys. **48** (2009) 07GK05.
2) Y. Yaoi, K. Yamamoto, T. Nakatsuji, T. Yanagitani, M. Matsukawa, K. Yamazaki, and A. Nagano: Jpn. J. Appl. Phys. **48** (2009) 07GK06.
3) A. Hosokawa: Jpn. J. Appl. Phys. **48** (2009) 07GK07.
4) M. Ohno, N. Ikeda, K. Ohira, and Y. Ogawa: Jpn. J. Appl. Phys. **48** (2010) 07HF27.
5) S. Hasegawa, Y. Nagatani, K. Mizuno, and M. Matsukawa: Jpn. J. Appl. Phys. **48** (2010) 07HF28.
6) F. Rupin, A. Saïed, D. Dalmas, F. Peyrin, S. Haupert, K. Raum, E. Barthel, G. Boivin, and P. Laugier: Jpn. J. Appl. Phys. **48** (2009) 07GK01.
7) C. G. Armstrong and V. C. Mow: J. Bone Joint Surg. **64** (1982) 88.
8) J. S. Wayne, K. A. Kraft, K. J. Shields, C. Yin, J. R. Owen, and D. G. Disler: Radiology **228** (2003) 493.
9) L. P. Li, W. Herzog, R. K. Korhonen, and J. S. Jurvelin: Med. Eng. Phys. **27** (2005) 51.
10) L. P. Li, R. K. Korhonen, J. Iivarinen, J. S. Jurvelin, and W. Herzog: Med. Eng. Phys. **30** (2008) 182.
11) P. C. Lin, D. A. Reiter, and R. G. Spencer: J. Magn. Reson. **201** (2009) 61.
12) M. J. Nissi, J. Rieppo, J. Töyräs, M. S. Laasanen, I. Kiviranta, M. T. Nieminen, and J. S. Jurvelin: Osteoarthritis Cartilage **15** (2007) 1141.
13) V. Mlynárik, I. Sulzbacher, M. Bittsanský, R. Fuiko, and S. Trattnig: J. Magn. Resonance Imaging **17** (2003) 440.
14) Q. Wang and Y. P. Zheng: Ultrason. Med. Biol. **35** (2009) 1535.
15) E. H. Chiang, T. J. Laing, C. R. Meyer, J. L. Boes, J. M. Rubin, and R. S. Adler: Ultrason. Med. Biol. **23** (1997) 205.
16) M. H. Lu, Y. P. Zheng, and Q. H. Huang: Ultrason. Med. Biol. **31** (2005) 817.
17) S. Z. Wang, Y. P. Huang, S. Saarakkala, and Y. P. Zheng: Ultrason. Med. Biol. **36** (2010) 512.
18) H. J. Nieminen, P. Julkunen, J. Töyräs, and J. S. Jurvelin: Ultrason. Med. Biol. **33** (2007) 1755.
19) J. K. F. Suh, I. Youn, and F. H. Fu: J. Biomech. **34** (2001) 1347.
20) J. Töyräs, M. S. Laasanen, S. Saarakkala, M. J. Lammi, J. Rieppo, J. Kurkijärvi, R. Lappalainen, and J. S. Jurvelin: Ultrason. Med. Biol. **29** (2003) 447.
21) S. G. Patil, Y. P. Zheng, and X. Chen: Ultrason. Med. Biol. **36** (2010) 1345.
22) H. J. Nieminen, S. Saarakkala, M. S. Laasanen, J. Hirvonen, J. S. Jurvelin, and J. Töyräs: Ultrason. Med. Biol. **30** (2004) 493.
23) S. Saarakkala, M. S. Laasanen, J. S. Jurvelin, K. Törrönen, M. J. Lammi, R. Lappalainen, and J. Töyräs: Osteoarthritis Cartilage **11** (2003) 697.
24) P. Kiviranta, E. Lammentausta, J. Töyräs, I. Kiviranta, and J. S. Jurvelin: Osteoarthritis Cartilage **16** (2008) 796.
25) A. S. Aula, J. Töyräs, V. Tiitu, and J. S. Jurvelin: Osteoarthritis Cartilage **18** (2010) 1570.
26) B. Pellaumail, A. Watrin, D. Loeuille, P. Netter, G. Berger, P. Laugier, and A. Saïed: Osteoarthritis Cartilage **10** (2002) 535.
27) S. Saarakkala, S. Z. Wang, Y. P. Huang, J. S. Jurvelin, and Y. P. Zheng: Ultrason. Med. Biol. **37** (2011) 112.
28) K. Hattori, K. Mori, T. Habata, Y. Takakura, and K. Ikeuchi: Clin. Biomech. **18** (2003) 553.
29) M. Fortin, M. D. Buschmann, M. J. Bertrand, F. S. Foster, and J. Ophir: J. Biomech. **36** (2003) 443.
30) Y. P. Zheng, H. J. Niu, F. T. A. Mak, and Y. P. Huang: J. Biomech. **38** (2005) 1830.
31) M. S. Laasanen, J. Töyräs, A. Vasara, S. Saarakkala, M. M. Hyttinen, I. Kiviranta, and J. S. Jurvelin: Osteoarthritis Cartilage **14** (2006) 258.
32) S. Saarakkala, J. Töyräs, J. Hirvonen, M. S. Laasanen, R. Lappalainen, and J. S. Jurvelin: Ultrason. Med. Biol. **30** (2004) 783.
33) C. Y. Tsai, C. L. Lee, C. Y. Chai, C. H. Chen, J. Y. Su, H. T. Huang, and M. H. Huang: Osteoarthritis Cartilage **15** (2007) 245.
34) J. Töyräs, T. Lyyra-Laitinen, M. Niinimaki, R. Lindgren, M. T. Nieminen, I. Kiviranta, and J. S. Jurvelin: J. Biomech. **34** (2001) 251.
35) L. Mancarella, M. Magnani, O. Addimanda, E. Pignotti, S. Galletti, and R. Meliconi: Osteoarthritis Cartilage **18** (2010) 1263.
36) T. Virén, S. Saarakkala, E. Kaleva, H. J. Nieminen, J. S. Jurvelin, and J. Töyräs: Ultrason. Med. Biol. **35** (2009) 1546.
37) N. Nitta, K. Homma, M. Misawa, K. Hoshi, S. Bu, and T. Shiina: Proc. IEEE Int. Ultrasonics Symp., 2010, p. 1400.
38) Y. Tanaka, Y. Saijo, Y. Fujihara, H. Yamaoka, S. Nishizawa, S. Nagata, T. Ogasawara, Y. Asawa, T. Takato, and K. Hoshi: J. Biosci. Bioeng. **113** (2012) 252.
39) V. C. Mow, S. C. Kuei, W. M. Lai, and C. G. Armstrong: J. Biomech. Eng. **102** (1980) 73.

# Model-Based Iterative Reconstruction Technique for Ultralow-Dose Chest CT

## Comparison of Pulmonary Nodule Detectability With the Adaptive Statistical Iterative Reconstruction Technique

Masaki Katsura, MD, Izuru Matsuda, MD, PhD, Masaaki Akahane, MD, Koichiro Yasaka, MD, Shohei Hanaoka, MD, PhD, Hiroyuki Akai, MD, PhD, Jiro Sato, MD, Akira Kunimatsu, MD, PhD, and Kuni Ohtomo, MD, PhD

**Purpose:** The purpose of this study was to evaluate whether model-based iterative reconstruction (MBIR) enables dose reduction over adaptive iterative reconstruction (ASIR) while maintaining diagnostic performance.
**Methods:** In this institutional review board–approved and Health Insurance Portability and Accountability Act–compliant study, 59 patients (mean [SD] age, 64.7 [13.4] years) gave informed consent to undergo reference-, low-, and ultralow-dose chest computed tomography (CT) with 64-row multidetector CT. The reference- and low-dose CT involved the use of automatic tube current modulation with fixed noise indices (31.5 and 70.44 at 0.625 mm, respectively) and were reconstructed with 50% ASIR-filtered back projection blending. The ultralow-dose CT was acquired with a fixed tube current-time product of 5 mA s and reconstructed with MBIR. Two radiologists evaluated 2.5- and 0.625-mm-slice–thick axial images from low-dose ASIR and ultralow-dose MBIR, recorded the pattern of each nodule candidate, and assigned each a confidence score. A reference standard was established by a consensus panel of 2 different radiologists, who identified 84 noncalcified nodules with diameters of 4 mm or greater on reference-dose ASIR (ground-glass opacity, n = 18; partly solid, n = 11; solid, n = 55). Sensitivity in nodule detection was assessed using the McNemar test. Jackknife alternative free-response receiver operating characteristic (JAFROC) analysis was applied to assess the results including confidence scores.
**Results:** Compared with the low-dose CT, a 78.1% decrease in dose-length product was seen with the ultralow-dose CT. No significant differences were observed between the low-dose ASIR and the ultralow-dose MBIR for overall nodule detection in sensitivity ($P = 0.48–0.69$) or the JAFROC analysis ($P = 0.57$). Likewise, no significant differences were seen for ground-glass opacity, partly solid, or solid nodule detection in sensitivity ($P = 0.08–0.65$) or the JAFROC analysis ($P = 0.21–0.90$).
**Conclusions:** Model-based iterative reconstruction enables nearly an 80% reduction in radiation dose for chest CT from a low-dose level to an ultralow-dose level, without affecting nodule detectability.

**Key Words:** model-based iterative reconstruction, adaptive statistical iterative reconstruction, radiation dose, pulmonary nodule detection

(*Invest Radiol* 2013;48: 206–212)

Lung cancer is the leading cause of death due to malignancy in most countries, with more than 1.3 million deaths estimated worldwide in 2008.[1] The disease is usually diagnosed at an advanced stage when the prognosis is poor, resulting in an overall 5-year survival rate of approximately 16%.[2] In contrast, the 5-year recurrence-free survival rate in patients with pathologically confirmed stage IA nonsmall cell lung cancer can be as high as 80%.[3,4] These data suggest that screening could help decrease mortality from lung cancer. There has been intense interest and intuitive appeal in low-dose computed tomography (CT) as a modality for lung cancer screening, and the National Lung Cancer Screening Trial (NLST), a large randomized control trial conducted in the United States, recently showed survival benefit in individuals who are at high risk for lung cancer (a 20% decrease in mortality from lung cancer) for low-dose screening CT over chest x-ray.[5]

Because of the screening nature of the examination and growing concerns about the potential harm that may derive from excess radiation, one key aim has been to keep the radiation dose delivered in previous lung cancer screening trials as low as technologically possible at the time.[6–8] The NLST involved 3 annual screenings with low-dose CT (average effective dose [ED], 1.5 mSv), resulting in a cumulative average ED of 4.5 mSv.[9] This may be acceptable among individuals who are at high risk for lung cancer, but if the feasibility of lung cancer screening CT is also to be investigated in the future for individuals who are at moderate or low risk for lung cancer, further reductions in radiation dose must be achieved while maintaining the diagnostic performance of CT for the detection of pulmonary nodules.

Several strategies have been used to enable dose reductions during CT acquisition, such as tube current modulation,[10] reduced tube voltage,[11] use of a higher pitch,[12] and noise reduction filters.[13] Use of an iterative reconstruction (IR) algorithm as an alternative to the standard filtered back projection (FBP) reconstruction algorithm is another strategy for dose reduction (see Appendix). One of the first IR algorithms released for clinical use was the adaptive statistical iterative reconstruction (ASIR) algorithm (GE Healthcare, Waukesha, WI). Adaptive statistical iterative reconstruction algorithm significantly reduces image noise compared with the FBP algorithm (see Appendix), provides dose-reduced clinical images with preserved diagnostic value,[14–24] and has been widely used for dose reduction in many CT systems. The recently developed model-based iterative reconstruction (MBIR) is a much more complex and advanced algorithm than ASIR is: it provides significant reductions in image noise and streak artifacts, significantly improves spatial resolution, and has the potential to allow further reductions in radiation dose without compromising image quality (see Appendix).[25,26] On the other hand, MBIR is also known for some unique imaging features, such as a pixelated blotchy appearance,[27,28] and the impact of these features on lesion detectability remains unclear. Up to this point, few studies have assessed the ability of MBIR to detect and localize lesions.[28,29] The purpose of this study was thus to evaluate whether MBIR enables further reductions in

**TABLE 1.** Patient Characteristics and CT Parameters

| | |
|---|---|
| Sex, men/women | 32/27 |
| Age, y | 64.7 (13.4) |
| Body weight, kg | 59.0 (14.1) |
| Acquisition mode | Helical |
| Tube voltage, kV(p) | 120 |
| Field of view, mm | 350* |
| Gantry rotation time, s | 0.5 |
| Table speed, mm per gantry rotation | 39.37 |
| Detector configuration, mm | 64 × 0.625 |
| Reconstructed section thickness, mm | 0.625 |
| Pitch | 0.984:1 |

Data represent mean (SD) for each value, unless indicated otherwise.

The main clinical indications for chest CT were as follows: follow-up for a pulmonary nodule (n = 15), abnormal results of chest radiography (n = 10), interstitial lung disease (n = 10), staging or restaging of known or suspected malignancy (n = 10), GGO (n = 3), obstructive pulmonary disease (n = 3), hemoptysis (n = 3), mediastinal mass (n = 2), sarcoidosis (n = 1), pulmonary tuberculosis (n = 1), and asbestosis (n = 1).

*Field of view was typically set at 350 mm, but it was adjusted according to patient size.

radiation dose over ASIR while maintaining diagnostic performance for the detection of pulmonary nodules.

## MATERIALS AND METHODS

This prospective clinical study was compliant with the Health Insurance Portability and Accountability Act guidelines and was approved by the Human Research Committee at our institution.

### Patients

The Radiology Information System was checked to identify patients scheduled for unenhanced standard-of-care clinical chest CT examinations at a single tertiary care center. Inclusion criteria for the present study were as follows: age of older than 18 years, patient scheduled for unenhanced standard-of-care CT examination of the chest, the ability to provide written informed consent, and the ability to hold his/her breath and remain still for at least 10 seconds. Patients who were unable to provide written informed consent, follow verbal commands for breath-holding, or remain still for the duration of CT acquisition were excluded. Women who were pregnant or were trying to get pregnant were also excluded. Each potential participant was given a detailed informed consent form that was written in simple

language about the objectives, methods, and risks of study participation. The study procedure, which involved acquisition of a reference-dose CT followed by low- and ultralow-dose CT (both discussed later in detail), was explained to the participants. The participants were also informed that the total radiation exposure from the reference-, low-, and ultralow-dose CT acquisitions would not exceed the radiation dose for the standard-of-care chest CT in our institution. The risks associated with study participation, particularly the possible influence on diagnostic performance, in which the reference dose in the present study was expected to be slightly lower compared with the radiation doses for the standard-of-care CT, were explained to the participants in simple language. The participants were also informed that they would not receive any remuneration or benefit from their participation in the study.

Between July 1, 2011, and July 28, 2011, a total of 113 consecutive eligible patients were prospectively identified. Nine patients declined to participate in the study, and 104 provided informed consent. After the CT acquisition, images were reviewed by the main author (M.K., with 4 years of imaging experience) and 30 patients who were associated with the following conditions that may hinder the interpretation of studies for pulmonary nodules were excluded: severe lung structural distortions (including the postoperative state), more than 10 nodules within 1 lobe (eg, nontuberculosis mycobacterial disease), numerous nodules throughout the lungs (eg, numerous lung metastases), or consolidation involving more than 1 segment. From the remaining 74 patients, images from 15 patients were selected using a random number table, which was used for training purposes (to understand the evaluation system) by 2 thoracic radiologists (K.Y. and S.H., with 3 and 10 years of experience, respectively), and subsequently eliminated from the remaining analyses. As a result, 59 patients were included in the final analysis. Demographic information for each patient is presented in Table 1.

### Computed Tomographic Data Acquisition

Unenhanced chest CT as the reference-dose CT followed by low- and ultralow-dose CT was performed using a 64-row multidetector CT system (Discovery CT750 HD; GE Healthcare, Waukesha, WI). All patients in the present study were able to undergo chest CT in the supine position with both arms elevated, with a single breath-hold for each acquisition. Imaging parameters for the reference-, low-, and ultralow-dose CT were held constant with the exception of radiation dose, as summarized in Table 1. To minimize positional differences between the 3 acquisitions, the time between each scan was kept to a minimum (about 10 seconds or less). To avoid contrast enhancement bias due to delays in imaging from the start of contrast injection, only the unenhanced CT images were included in the present study. The CHEST kernel (a proprietary kernel of GE Healthcare, Waukesha, WI) was used
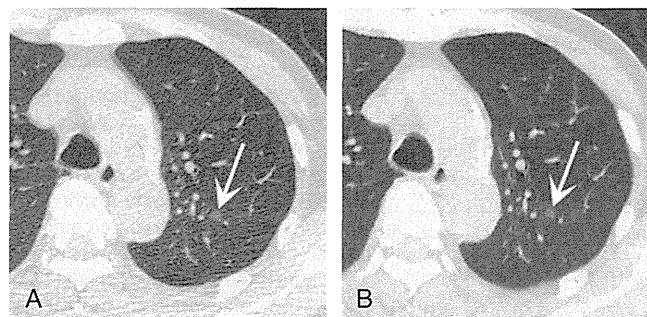


**FIGURE 1.** Imaging results of a 79-year-old man (weight, 64 kg): A, Low-dose CT (DLP, 64.2 mGy-cm) reconstructed with ASIR. B, Ultralow-dose CT (DLP, 15.4 mGy-cm) reconstructed with MBIR. The prominent streak artifact from the shoulders on the low-dose ASIR (A) interferes with the adequate visualization of the GGO nodule in the left upper lobe (arrow), which was missed by both radiologists. In the ultralow-dose MBIR (B), the nodule is clearly depicted (arrow) and was identified by both radiologists. The images are shown in lung window settings (WW, 1,500 HU; WL, −600 HU).
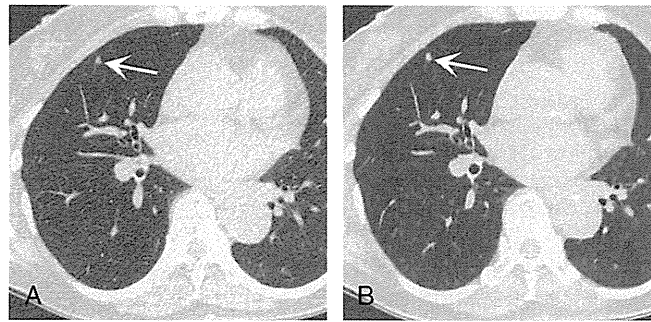
**FIGURE 2.** Imaging results of a 64-year-old woman (weight, 52 kg): A, Low-dose CT (DLP, 36.4 mGy-cm) reconstructed with ASIR. B, Ultralow-dose CT (DLP, 14.0 mGy-cm) reconstructed with MBIR. Both images provide adequate visualization of the solid nodule in the right middle lobe (arrows), which was identified by both radiologists.

for image reconstruction. This kernel is equivalent to the LUNG kernel (a proprietary kernel of GE Healthcare, Waukesha, WI) for depiction of the lung and equivalent to the SOFT-TISSUE kernel (a proprietary kernel of GE Healthcare, Waukesha, WI) for depiction of mediastinal soft-tissue structures.[30,31] All images were reconstructed with 0.625-mm–thick axial slices, and the images with increased slice thickness of 2.5 mm (by averaging) were also used for interpretation as necessary, in accordance with the NLST protocol.[5] The images with coronal/sagittal reformats were not used for evaluation in this study because the preliminary results of our phantom experiments indicated that MBIR and ASIR behave differently in image noise when reformatted into coronal and sagittal slices (I. Matsuda, unpublished data, November 2012).

## Radiation Dose Setting

Both reference- and low-dose CT protocols involved the use of automatic tube current modulation (Auto mA 3D; GE Healthcare). The operator-selected noise index (NI) level modulates the tube current during gantry rotation to achieve a predicted average statistical noise level in the images of the reconstruction slice thickness specified. In the present study, a fixed NI of 31.5 at 0.625 mm was used for the reference-dose CT, which, theoretically, should achieve the same radiation dose for the reference-dose chest CT described in the radiology literature.[14,32] As for the low-dose CT (NI of 70.44 at 0.625 mm), we referred to the mean ED for the low-dose CT described in the NLST (1.5 mSv),[9] which is about one-fifth of the radiation dose for the reference-dose chest CT described in the radiology literature.[14,32] The ultralow-dose CT was acquired using a fixed tube current-time product of 5 mA s.

## Image Reconstruction

The images for the reference- and low-dose CT were reconstructed with blending of 50% FBP and 50% ASIR image data (ASIR50). The blending factor of 50% was chosen on the basis of the literature[16,17] and the recommendations of the vendor. The images for the ultralow-dose CT were reconstructed with MBIR. Blending with FBP does not apply to MBIR because this is a pure IR technique (see Appendix). Thus, 3 axial image data sets (reference-dose ASIR, low-dose ASIR, and ultralow-dose MBIR) were generated for each patient. The low-dose ASIR and the ultralow-dose MBIR were used for image interpretation (Figs. 1 and 2), after removing patient information to allow blinded evaluation. The reference-dose ASIR was used for establishing a reference standard.

## Image Interpretation

Two thoracic radiologists (K.Y. and S.H.) independently evaluated the ultralow-dose MBIR images from the 59 patients (ultralow-dose MBIR session), then evaluated the low-dose ASIR images (low-dose ASIR session), using a commercial software (EV Insite; PSP

Corporation, Tokyo, Japan). The image interpretation was performed using both 2.5- and 0.625-mm–thick axial images as necessary, in accordance with the NLST protocol.[5] The images in each reading session were presented in random order to each reader. To minimize recall bias, the 2 reading sessions were separated by 4 weeks. Both radiologists already had 3 years of experience with ASIR images at the time of the present study because of its introduction into our department in January 2009. They had little experience with MBIR images at the time of the study, although they became familiar with MBIR images through the training session. The radiologists, who were blinded to patient data and clinical information, were instructed with the following: to identify all noncalcified pulmonary nodules with long-axis diameters of 4 mm or greater using a procedure similar to that used in routine clinical practice, using a caliper on the monitor; to report the location and radiologic pattern (ground-glass opacity [GGO], partly solid, or solid) of each candidate nodule, and to assign a confidence level for each nodule using a 4-point scale (1, nodule probably not present; 2, nodule presence equivocal; 3, nodule probably present; 4, nodule definitely present), according to the free-response receiver operating characteristics (FROC) paradigm. For each session, the radiologists were given an unlimited amount of time to independently analyze the images. In addition to the default preselected lung window settings (window width [WW], 1500 Hounsfield units [HU]; window level [WL], −600 HU), the radiologists were allowed to change the WW and WL for ease of assessment.

Some of the images used for evaluating pulmonary nodule detection in this study were also used for assessing image quality characteristics in a previous study.[28] The previous study was conducted merely for image quality assessment and is completely different from the present study in nature. The present study specifically focused on diagnostic performance for the detection of pulmonary nodules by 2 different thoracic radiologists, neither of whom were involved in the image interpretation process for the previous study.

## Reference Standard

A consensus panel of 2 different radiologists (I.M. and H.A., with 6 and 8 years of experience, respectively) independently interpreted the entire set of images from the reference-dose ASIR and identified noncalcified pulmonary nodules with diameters of 4 mm or greater, in accordance with the positive findings in the NLST.[5] Interpretation of images for establishment of the reference standard occurred both as a free search through the CT sections and as a directed analysis of all candidate nodules originally identified by the previous 2 radiologists (K.Y. and S.H.). The panel members (I.M. and H.A.), without knowledge of the source of detection of the candidate nodules, assessed each candidate and arrived at a final consensus decision as to whether the finding represented a nodule (true-positive finding) or not (false-positive finding). In addition, the long-axis diameter of each